

## Imaging activated T cells predicts response to cancer vaccines

Israt S. Alam, ... , Ronald Levy, Sanjiv S. Gambhir

*J Clin Invest.* 2018. <https://doi.org/10.1172/JCI98509>.

Research Article In-Press Preview Immunology Oncology

In situ cancer vaccines are under active clinical investigation due to their reported ability to eradicate both local and disseminated malignancies. Intratumoral vaccine administration is thought to activate a T cell mediated immune response, which begins in the treated tumor and cascades systemically. We describe a positron emission tomography tracer ( $^{64}\text{Cu}$ -DOTA-AbOX40) that enabled non-invasive and longitudinal imaging of OX40, a cell surface marker of T cell activation. We report the spatiotemporal dynamics of T cell activation following in situ vaccination with CpG oligodeoxynucleotide, in a dual tumor bearing mouse model. We demonstrate that OX40 imaging could predict tumor responses at day 9 post treatment based on tumor tracer uptake at day 2, with higher accuracy than both anatomical and blood-based measurements. These studies provide key insights into global T cell activation following local CpG treatment and indicate that  $^{64}\text{Cu}$ -DOTA-AbOX40 is a promising candidate for monitoring clinical cancer immunotherapy strategies.

Find the latest version:

<https://jci.me/98509/pdf>



## Imaging activated T cells predicts response to cancer vaccines

Israt S. Alam<sup>1,2\*</sup>, Aaron T. Mayer<sup>1,2,3\*</sup>, Idit Sagiv-Barfi<sup>4</sup>, Kezheng Wang<sup>1,5</sup>, Ophir Vermesh<sup>1,2</sup>,  
Debra K. Czerwinski<sup>4</sup>, Emily M. Johnson<sup>1,2,6</sup>, Michelle L. James<sup>1,2,6</sup>, Ronald Levy<sup>4</sup> and  
Sanjiv S. Gambhir<sup>1,2</sup>

<sup>1</sup>*Department of Radiology, Stanford University, Stanford, CA, 94305, USA*

<sup>2</sup>*Molecular Imaging Program at Stanford, Stanford University, Stanford, CA, 94305, USA*

<sup>3</sup>*Department of Bioengineering, Stanford University, Stanford, CA, 94305, USA*

<sup>4</sup>*Division of Oncology, Department of Medicine, Stanford University, Stanford, CA, 94305, USA*

<sup>5</sup>*Department of Radiology, the Fourth Hospital of Harbin Medical University and Molecular  
Imaging Center of Harbin Medical University, Harbin, China*

<sup>6</sup>*Department of Neurology and Neurological Sciences, Stanford University, Stanford, CA, 94305,  
USA*

*\* Authors contributed equally.*

**Keywords:** OX40, T cells, positron emission tomography, in situ vaccine, CpG oligodeoxynucleotide (CpG ODN), cancer immunotherapy model, predicting immune response

Word count main text (not incl. references and figure legends): 6366

**Corresponding author: Sanjiv Sam Gambhir**, MD, PhD; Chair, Department of Radiology, Director, Molecular Imaging Program at Stanford (MIPS); Professor, Department of Radiology, Stanford University, The James H Clark Center, 318 Campus Drive, East Wing 1st Floor, Stanford, CA 94305; Phone: 650-725-2309; Email: [sgambhir@stanford.edu](mailto:sgambhir@stanford.edu)

## **ABSTRACT**

In situ cancer vaccines are under active clinical investigation due to their reported ability to eradicate both local and disseminated malignancies. Intratumoral vaccine administration is thought to activate a T cell mediated immune response, which begins in the treated tumor and cascades systemically. We describe a positron emission tomography tracer ( $^{64}\text{Cu}$ -DOTA-AbOX40) that enabled non-invasive and longitudinal imaging of OX40, a cell surface marker of T cell activation. We report the spatiotemporal dynamics of T cell activation following in situ vaccination with CpG oligodeoxynucleotide, in a dual tumor bearing mouse model. We demonstrate that OX40 imaging could predict tumor responses at day 9 post treatment based on tumor tracer uptake at day 2, with higher accuracy than both anatomical and blood-based measurements. These studies provide key insights into global T cell activation following local CpG treatment and indicate that  $^{64}\text{Cu}$ -DOTA-AbOX40 is a promising candidate for monitoring clinical cancer immunotherapy strategies.

## INTRODUCTION

The field of immuno-oncology has experienced rapid and exciting growth, benefiting from the development of intricate adoptive cell therapies (1), numerous monoclonal antibodies (with clinical approval of over twenty) and a deeper understanding of the immune-suppressive tumor microenvironment now deemed a hallmark of cancer (2-4). Immunotherapies, which function by priming the patient's immune system to recognize and destroy malignant cells have greatly altered traditional treatment paradigms. Their variable successes in the clinic have invigorated interest in non-invasive and longitudinal monitoring of immune responses with the aim of understanding why certain therapies succeed whilst others fail to deliver durable clinical responses. With the complex and varying spatiotemporal signatures of immune modulation, it has proved challenging to monitor and predict response to cancer immunotherapy using standard imaging practices. Current clinical practice, which includes magnetic resonance (MR) or computed tomography (CT) derived anatomical measurements, often yields limited or potentially misleading data (5). With the use of MR and CT, clinicians face the challenge of distinguishing between increases in lesion-size due to disease progression and 'pseudoprogession' caused by an influx of tumor-infiltrating immune cells, usually a positive indicator of treatment response. Limitations to the *Response Evaluation Criteria in Solid Tumors* (RECIST) have prompted the development of specific *immune related Response Criteria* (irRC) (6, 7). However, even these criteria are unable to provide an early indication of therapy efficacy such that 8-12 weeks may pass before an initial response assessment can be performed. Another limitation of these criteria is that they do not provide any biological insight. Excisional biopsies taken for histopathological assessment, can yield biological information and corroborate anatomical imaging, but are invasive, challenging to apply and can be unreliable due to intrinsic tumor heterogeneity. Thus, there is a pressing need to develop predictive and prognostic readouts that can illuminate our understanding of response to immunotherapies, both in terms of dynamic alterations in immune function and clinical outcome.

Positron emission tomography (PET) imaging is a highly sensitive and quantitative clinical imaging modality with the potential to enable non-invasive real-time visualization of dynamic immune responses. An array of small molecule metabolic PET radiotracers has been developed and characterized to date for applications in immune cell imaging. For example, <sup>18</sup>F-Fluorodeoxyglucose (<sup>18</sup>F-FDG), the most widely used clinical PET tracer, has principally been used to assess the efficacy of traditional non-targeted chemotherapies, but has also been used extensively to evaluate inflammation in the clinic (8, 9). A major challenge to delineating immunotherapy response, however, is that <sup>18</sup>F-FDG suffers from relatively high uptake in both tumor infiltrating T cells and cancer cells (10), as do other small molecule metabolic tracers including 3'-deoxy-3'-[<sup>18</sup>F]-fluorothymidine (<sup>18</sup>F-FLT), 1-(2'-deoxy-2'-[<sup>18</sup>F]fluoro-β-d

arabinofuranosyl)cytosine ( $^{18}\text{F}$ -AraC) (11) and 2'-deoxy-2'-[ $^{18}\text{F}$ ]fluoro-9- $\beta$ -D-arabinofuranosyl guanine ( $^{18}\text{F}$ -AraG) (11, 12). Reporter gene strategies, such as the use of herpes simplex virus type 1 thymidine kinase (HSV1-*tk*) in conjunction with the PET tracer 9-[4-[ $^{18}\text{F}$ ]-fluoro-3-(hydroxymethyl)butyl]guanine ( $^{18}\text{F}$ -FHBG), represent a powerful way to monitor trafficking and survival of adoptive immune cell therapies. These strategies have been evaluated clinically but require *ex vivo* manipulation of cells which is not always feasible (13).

ImmunoPET - a direct imaging strategy that combines PET isotopes with targeting antibodies, engineered fragments or binders, can overcome many of the challenges associated with small molecule radiotracers. Importantly, immunoPET offers increased specificity for immune sub-sets and functional states through the targeting of cell-surface markers (14). The presence of CD8<sup>+</sup> T cells in tumor biopsies is usually associated with favorable therapeutic response in patients receiving immunotherapy (15, 16) and thus has fueled the development of a range of CD8-targeted PET probes (17-19). Whilst the infiltration of CD8<sup>+</sup> T cells has been a recent major focus for the imaging community, the role of CD4 population is increasingly being reported (20, 21). A PET probe that could potentially report on both CD8 and CD4 populations could therefore provide a more comprehensive picture. While CD3 targeted probes can capture the dynamics of both phenotypic subsets, this biomarker still fails to report on the activation state of T cells which has been highlighted as a critical determinant of treatment success in oncology. Delineating cellular states such as activation and exhaustion, could enable more accurate prediction of prognostic outcomes than reporting on the presence of tumor infiltrating immune cells alone, which may well be present but rendered anergic. Indeed, imaging the dynamics of activated immune states is currently being explored by many groups pre-clinically (19, 22).

Given the explicit need for improved imaging biomarkers of response to immunotherapy and the central role of activated CD8<sup>+</sup> and CD4<sup>+</sup> T cells in this context, our group performed a thorough literature and database query and identified OX40 (CD134) receptor as a highly promising biomarker candidate. A member of the tumor necrosis factor (TNF) receptor superfamily, OX40 binds the ligand OX40L, found on activated antigen presenting cells (APCs), resulting in recruitment of TNF-receptor associated factors (TRAFs), formation of a T cell receptor (TCR)-independent signaling complex and downstream activation of NF-kappaB (23). The resultant production of cytokines such as IL-2 and IFN- $\gamma$  promotes survival, proliferation and activation of T cells. OX40 expression is restricted to antigen-specific activated T cells, in contrast to other activation markers (i.e. CD25, CD44) which are associated with many cell types.

Based on these reports of OX40 as a highly specific biomarker of activated T cells, we set out to validate these findings by developing a PET imaging agent capable of detecting its expression. We

report here for the first time, the development of an antibody-based PET imaging agent capable of non-invasive and specific- detection of OX40 for monitoring activated T cell responses in a clinically relevant in situ cancer vaccine model. Furthermore, by integrating simple machine learning approaches and OX40 PET imaging derived biomarkers, we successfully predict tumor response to in situ vaccines at earlier timepoints and with much greater accuracy than anatomic or blood-based biomarker strategies alone.

## RESULTS

### Validation of OX40 as a sensitive and specific indicator of T cell activation

To begin, we sought to validate OX40 as a potential biomarker of activated T cells in culture. Fluorescence-activated cell sorting (FACS) analysis of murine T cells stimulated with Phorbol 12-myristate 13-acetate (PMA) and Ionomycin or with CD3/CD28 specific antibody coated Dynabeads, showed a significant ( $p < 0.001$ ) increase in OX40 expression versus resting cells. Importantly, we also confirmed the selective upregulation of OX40 on activated human T cells. The expression of OX40 on murine and human T cells correlated well with other established T cell activation markers including CD44, CD25 and CD69 (24, 25) (Figure 1A). A closer look at the OX40<sup>+</sup> cells revealed that the population was comprised of both CD4<sup>+</sup> and CD8<sup>+</sup> T cell subsets (Figure 1B).

To modify the murine OX40 antibody for radiolabeling, DOTA chelate conjugation was initially optimized using 5, 10 or 15 fold-excess of chelate to antibody in overnight reactions at 4°C (Figure S1A). Post conjugation, the reactions were quenched and analyzed using mass spectrometry to confirm the average number of chelates per antibody molecule. To prevent over-modification of the antibody and associated loss of immune-reactivity, a 5-fold DOTA excess was chosen for all subsequent batches of conjugate produced, which yielded an average of 2-3 DOTAs per antibody (Figure S1B). To test immunoreactivity, we performed cell binding studies with activated murine T cells, which showed that binding of DOTA-AbOX40 to cells was comparable to unconjugated antibody (Figure S1C, left panel). Furthermore, using a competitive cell binding assay we were able to show that the endogenous OX40 ligand (OX40L) and the mAb used for tracer development do not compete, thus minimizing the potential effects of OX40L expression *in vivo*, on radiotracer sensitivity (Figure S1C, right panel). SEC-HPLC chromatograms of the immune-conjugate at 220nm showed a principal peak at 8 minutes corresponding to DOTA-AbOX40, as confirmed by SDS-PAGE (Figure S1D). Purification of the final copper-labeled immunoconjugate (<sup>64</sup>Cu-DOTA-AbOX40) was followed by radio-HPLC analysis which, in conjunction with TLC, confirmed high radiochemical purity (99%) (Figure S1E). Final characterization of the radiotracer (<sup>64</sup>Cu-DOTA-AbOX40) revealed a specific activity of 5-10 $\mu$ Ci/ $\mu$ g (Figure S1F).

To assess the specificity of the radiotracer, we performed cell binding assays using resting, PMA/Ionomycin and Dynabead activated murine T cells. Cells were incubated with the radiotracer for 30 minutes, washed thoroughly and analyzed for cell-associated radioactivity using a gamma counter. <sup>64</sup>Cu-DOTA-OX40 binding correlated well with cell activation and OX40 expression as measured by flow cytometry (Figure 1C and Figure 1D). Resting murine T cells which showed negligible OX40 expression, exhibited the least binding to the radiotracer. T cell activation by

Dynabeads (simulating APC stimulation), is known to be a more potent stimulus for activating T cells than PMA/Ionomycin. Indeed, Dynabead activated T cells showed greatest target expression and correspondingly highest binding of the radiotracer (Figure 1D). Importantly, uptake was high in activated T cells and low in resting, blocked and OX40 knockout T cells, with minimal non-specific binding in these samples. We also observed minimal non-specific uptake across a panel of murine suspension and adherent cancer lines, providing further evidence for the high specificity of OX40 as a biomarker of activated T cells (Figure 1E).

### **Characterization of OX40 as a biomarker of activated T cells in an in situ adjuvant vaccine model**

To establish and characterize OX40 as a biomarker of activated T cell immune response in living subjects, we chose a model that recapitulates an in situ tumor adjuvant vaccination strategy currently being tested in phase I clinical trials (26, 27). We employed a murine two-tumor site subcutaneous A20 lymphoma model in which an intratumoral vaccine adjuvant, CpG oligonucleotide (ODN) was administered into only one of the tumors. CpG ODNs are ssDNA fragments containing unmethylated cytosine-guanine sequence motifs, a signature of microbial DNA, that bind to Toll-like receptors (TLR) present on APCs and trigger intracellular signaling and immune activation (28). Due to its ability to elicit the innate immune component as well as antigen-specific T cell responses, CpG has been explored clinically as a vaccine adjuvant and in conjunction with chemotherapy and radiotherapy (29).

Here, mice bearing dual A20 tumors (~60-80mm<sup>3</sup>) were administered CpG (50µg in 50µl PBS) or vehicle (50µl PBS) intratumorally on day 0, 2, and 4 in the tumor site near the left shoulder. The distal tumor on the right shoulder remained untreated (Supplementary Figure 2). We hypothesized that in situ vaccination with CpG would repolarize the locally treated tumor environment and induce an activated T cell response (Figure 2A). Tumor growth curves (volume mm<sup>3</sup>, n=7-8/group) indicated that CpG in situ vaccination led to a statistically significant ( $p < 0.0001$ , Two-way ANOVA) therapeutic response in the treated tumor as early as day 7 and delayed tumor growth in the distal untreated tumor, evident by day 9 ( $p < 0.01$ , Two-way ANOVA) (Figure 2B). This data suggested that the local immune response triggered by CpG had the potential to cascade systemically, in line with previous reports (26). This provided us the opportunity to characterize the spatiotemporal expression of OX40 as a potential biomarker of activated T cell immune response dynamics following in situ CpG vaccination. We chose day 2 post therapy, where no changes in tumor volume were yet evident, and day 9, where treatment cohorts exhibited clear response stratification based on a visual tumor volume reduction, as our early and late analysis time points respectively.

At the early timepoint, flow cytometry analysis revealed increased OX40 expression in the treated tumor and a statistically significant increase in frequency of OX40<sup>+</sup> CD3<sup>+</sup> T cells following CpG in-situ vaccination in the treated tumor draining lymph node compared to both the untreated sites ( $p < 0.05$ ) and vehicle cohorts ( $p < 0.01$ ) (Figure 2C-D, Supplementary Figure 3A-B). Selective upregulation of OX40 at the treatment sites alone suggested in situ CpG vaccination triggered a local induction of cellular immune response. Changes in OX40<sup>+</sup> CD3 frequency preceded a relative increase in the overall proportion of CD3<sup>+</sup> T cells within CpG-treated tumors. Interestingly, CpG vaccination did not cause significant changes in the relative frequencies of CD4<sup>+</sup> helper or CD8<sup>+</sup> cytotoxic T cell subsets within the tumor (Supplementary Figure 3C-D).

Given reports that OX40 expression has been found in several other cell types (30), including constitutive expression on FoxP3<sup>+</sup> T regulatory cells in mice but not humans, we examined the phenotype of cells expressing OX40 in our model. Visualization of the high-dimensional single-cell data was performed using ViSNE (described in supplemental methods). ViSNE maps depicted OX40<sup>+</sup> cells to be highly restricted to clusters associated with T cells (Figure 2E) and more specifically, CD4 helper T cells. Other potential biomarkers of T cell activation including CD44, CD25, and PD-1 exhibited much less restriction to T cell associated clusters consistent with their known roles on a variety of other cellular subsets (Supplementary Figure 4A). OX40<sup>+</sup> CD4 T cells in the tumor and tumor draining lymph nodes were also double positive for the activation markers CD44 and CD25 (Supplementary Figure 4B-C). Furthermore, the expansion of CD44<sup>+</sup>CD25<sup>+</sup>OX40<sup>+</sup> CD3<sup>+</sup> T cells observed upon CpG in-situ vaccination represented a non-regulatory FoxP3<sup>-</sup> CD4<sup>+</sup> T cell subset (Supplementary Figure 4D). Our analyses therefore suggest that OX40 is predominantly a biomarker of a highly activated effector T cell subset in this mouse model and that CD4<sup>+</sup> T cells play an important role following in situ vaccination with CpG.

At the late timepoint, CpG-treated tumors exhibited a significant reduction in tumor volume. Correspondingly, OX40 expression returned to baseline (Figure 2C-D). While heightened OX40 expression was observed in the distal untreated TDLN of a few CpG-treated mice, detectable increases in OX40 expression in the untreated tumor failed to emerge on average, consistent with a weak therapeutic response at these sites. At the late time point, secondary lymphoid organs such as the spleen appeared enlarged and exhibited an increase in OX40<sup>+</sup> CD3<sup>+</sup> T cell frequency ( $p < 0.001$ ) (Figure 2F). Luminex<sup>®</sup> analysis revealed that robust inflammatory cytokine signatures present in the blood at day 2 following in situ vaccination with CpG had begun to taper by day 9, with several CpG-treated mice no longer showing upregulation of inflammatory cytokines (Figure 2G, Supplementary Figure 5, Supplementary Figure 6).

Taken together, these findings highlight the complex immune response following in situ vaccination with CpG. OX40<sup>+</sup> activated T cells exhibited spatiotemporal varying signatures in response to treatment. Recognizing that biopsies are invasive and cannot adequately sample the heterogeneity in immune response across subjects, we sought to evaluate OX40 ImmunoPET as a means of non-invasively monitoring activated T cell dynamics at the systems level.

### **Noninvasive imaging of OX40 to assess the spatiotemporal dynamics of activated T cells following in situ vaccination**

To assess the ability of <sup>64</sup>Cu-DOTA-AbOX40 to capture the dynamics of OX40<sup>+</sup> T cells and to further elucidate the critical role they play in this therapy model (31), we performed longitudinal ImmunoPET imaging studies. PET images acquired at 24 hours after tracer injection interestingly showed pronounced <sup>64</sup>Cu-DOTA-AbOX40 signal in the tumor draining lymph node (TDLN) of tumor bearing mice (Figure 3, Supplementary Figure 7) which was not observed in peripheral lymph nodes of these mice or naïve mice (data not shown). This signal is likely attributed to T cells which have been exposed to antigen draining from the local tumor or a regulatory T cell compartment that is present at baseline. Upon treatment with CpG, PET imaging (post-treatment Day 2) revealed a local response to the in situ vaccination. We observed a significant enhancement of the PET signal in the CpG vaccine treated tumor (56%↑, p<0.01) and associated TDLN compared with both the vehicle-treated tumor and the distal untreated sites. This observation corroborated the expansion of the OX40<sup>+</sup> CD4<sup>+</sup> T cell effector subset we observed during our FACS studies.

Histological analysis of Day 2 treated tumors, supports the PET images whereby OX40 expressing cells were clearly observed in tumors receiving CpG treatment, whereas vehicle-treated tumors exhibited overall low numbers of double positive CD3 OX40 stained cells which likely represented T-regs (Supplementary Figure 8). Histology revealed a heterogeneous distribution of CD3<sup>+</sup> T cell infiltration in both CpG and vehicle tumors, highlighting the difficulty of assessing tumors based on T cell numbers and penetration alone.

At day 9 post treatment, we observed enhancement of the <sup>64</sup>Cu-DOTA-AbOX40 PET signal in the spleen (247.9%↑, p<0.0001), and in a small number of distal untreated TDLNs (Figure 3C-D). Given that the imaging findings closely corroborate the histology and flow cytometry analysis, the evidence strongly suggests that <sup>64</sup>Cu-DOTA-AbOX40 is capable of noninvasively monitoring the dynamics of OX40 T cells.

To quantify these trends, we performed ROI analysis of multiple organs visualized on PET images as well as *ex vivo* biodistribution analysis. ROI analysis on Day 2 revealed a distinct pattern of

organ uptake in CpG-treated mice compared to vehicle-treated controls (Figure 4A). Moreover, unsupervised hierarchical clustering could accurately distinguish these two groups, based on their uptake signatures (Supplementary Figure 9A). Notably, greater accumulation of the tracer was observed in CpG-treated tumors ( $10.29 \pm 0.74$  %ID/g,  $p < 0.0001$ ) and associated TDLNs ( $12.92 \pm 1.15$  %ID/g) versus vehicle-treated tumors (Figure 4A, Supplementary Figure 9B). To better understand the pharmacokinetics of  $^{64}\text{Cu}$ -DOTA-AbOX40, PET signals at key sites were plotted over time (Figure 4B). Following administration, the radiotracer was observed to accumulate in all tumors over 24 hours; however, the CpG-treated tumors exhibited a comparatively greater increase than vehicle-treated tumors ( $p < 0.05$ ). In contrast to the accumulation observed in tumors, the radiotracer exhibited clearance from the heart, liver and kidney, with no significant difference in clearance from these tissues between the two groups.

*Ex vivo* analysis of tissues at Day 2 also corroborated the imaging data (Supplementary Figure 9B-C). A significant increase in radioactivity was observed between treated tumors in experimental versus vehicle groups ( $p < 0.01$ ), with no significant differences in the distal untreated tumors between the two groups (Figure 4C). Differences observed between groups appeared to be local at this timepoint with no splenic involvement (Figure 4D). Blocking with cold antibody significantly reduced  $^{64}\text{Cu}$ -DOTA-AbOX40 uptake in the CpG-treated tumors as well as in the TDLNs, in this case, the axillary lymph nodes (AX LN) (Supplementary Figure 9B), confirming specificity of the PET signal for OX40. We observed a strong inverse correlation between tumor response (measured as a decrease in tumor volume) and tracer uptake in tumors at Day 2 (Figure 4E).

At Day 9, however, tracer uptake was no longer increased in the CpG-treated tumors relative to vehicle-treated tumors, while the spleens of the experimental group showed a significant increase in tracer accumulation compared with the vehicle group (Figure 4F-G). The signal in the CpG-treated TDLN (Left Ax) showed persistent enhancement, and as before, only rarely did the tracer enhance in the non-treated TDLNs (Right Ax) (Figure 4H).

To thoroughly test the specificity of our imaging agent, we employed additional controls (Supplementary Figure 9 D-E). For example, in one experiment, we injected a non-radiolabeled isotype control antibody, prior to radiotracer administration in order to rule out non-specific uptake of the radiotracer resulting from Fc receptor upregulation in response to CpG treatment. The lack of blocking in the CpG-treated tumors of mice pre-treated with isotype control, demonstrates that Fc receptors do not contribute significantly to tracer binding in the tumor and TDLN, and that the tracer accumulation occurs principally through engagement with OX40. In a separate experiment, an OX40 knockout (KO) melanoma tumor-bearing mouse model was treated with the same vaccine strategy. Unlike OX40 wild type mice, which showed a statistically significant 1.4-1.5 fold increase

( $p < 0.05$ ) in tracer uptake in CpG-treated vs distal untreated tumors, OX40 KO mice failed to show this trend despite responding to the CpG therapy (Supplementary Figure 9E).

### **Classification and prediction of tumor response to in situ vaccination utilizing in vivo OX40 imaging biomarkers**

Having established that  $^{64}\text{Cu}$ -DOTA-AbOX40 could report on activated T cell immune responses with high sensitivity and specificity, our final goal was to compare and contrast the ability of blood and image derived biomarkers to monitor and predict tumor response. We therefore performed profiling of blood cytokines and image ROIs to identify biomarkers that correlate with tumor response (Figure 5A). Individual cytokines and cytokine sets showed weak correlation with tumor response (Table 1), whereas imaging biomarkers alone exhibited improved correlation. Incorporating multiple PET imaging biomarkers into our generalized linear regression model yielded a statistically significant correlation with therapeutic response [ $r^2 = 0.674$ ,  $p = 8.425\text{E-}5$ ] (Table 1).

We further set out to determine whether *early* (day 2) ImmunoPET images could provide insight into *late* (day 9) therapeutic response. Anatomical measurements revealed that early tumor response to CpG is not a strong predictor of late therapeutic response ( $r^2=0.40$ ,  $p=0.18$ ), with some tumors showing initial regression followed by growth and others presenting with pseudo-progression (Figure 5B, Table 2). On the other hand, early ImmunoPET tracer uptake in tumors was strongly correlated with late therapeutic response in CpG-treated mice ( $r^2 = 0.76$ ,  $p = 0.02$ ) (Figure 5C, Table 2). Due to large discrepancies in tumor volume between CpG and vehicle cohorts, we initially considered them independently. As expected, vehicle-treated mice showed a correlation between early and late anatomical measurements ( $r^2=0.74$ ,  $p = 0.11$ ), while early ImmunoPET tracer uptake in tumors did not correlate with late response ( $r^2=0.23$ ,  $p=0.33$ ). Incorporating multiple OX40 image derived biomarkers into our linear regression, provided us with a robust general model ( $r^2=0.74$ ,  $p=0.08$ ) to assess response independent of treatment cohort.

We finally sought to determine whether our ImmunoPET images could enable accurate classification of therapeutic responders vs non-responders. We stratified mice into two response groups with the help of unsupervised hierarchical clustering (Figure 5D). We built a simple k-means classifier based on our imaging biomarkers, which we had previously identified to correlate well with therapeutic response (Figure 5E). We trained the classifier on a subset of mice ( $n=16$ ), and tested the classifier on all cohorts of mice included in our study ( $n=46$ ). The model performed well with 83% accuracy, 82% specificity, and 85% sensitivity in the total cohort (Table 3). Overall, we view this as an initial and promising proof of principle that OX40 ImmunoPET image derived

biomarkers can not only monitor, but classify responders at early time points following therapy.

## DISCUSSION

Due to the relative ease of ImmunoPET tracer development, it is feasible to build a clinical toolbox of tracers useful for predicting and monitoring responses to different cancer immunotherapies. Here we highlight the development cycle starting from biomarker identification (OX40) and tracer development ( $^{64}\text{Cu}$ -DOTA-Ab-OX40) to biomarker characterization and tracer validation in mouse models receiving immunotherapy treatment. Moreover, we demonstrate the potential clinical utility of this tracer by illustrating its predictive power in therapeutic mouse models, a critical step often omitted from many preclinical imaging studies.

As the field evolves and an imaging toolbox to assess immunotherapies is developed, careful biomarker selection is paramount. Small molecule tracers, as previously mentioned, have focused on metabolic pathways that are not immune cell specific. Nucleoside analogs like  $^{18}\text{F}$ -FLT,  $^{18}\text{F}$ -AraC and  $^{18}\text{F}$ -AraG have all been explored for immune cell imaging (11, 12, 32). The latter for instance exhibits increased specificity for activated T cells (33) and recently showed utility in the detection of these cells in murine models of acute Graft Versus Host Disease and Arthritis (34). In the context of cancer however, with the uptake mechanism of these metabolic tracers being dependent on elevated levels of nucleoside transporters and DNA salvage pathway enzymes, imaging of tumor infiltrating T cells could potentially be confounded by uptake in certain cancers that also exhibit the same features. Meanwhile, previous ImmunoPET strategies have struggled to demonstrate utility because the presence of infiltrating immune cell subsets does not on its own correlate well with immune response (18). In addition, while imaging metrics of cell infiltration have been developed, they may encounter difficulties when applied in the clinic due to heterogeneity, size and shape of spontaneous tumors. Imaging markers that directly reflect the functional status of specific cells have the potential to be more predictive, providing that expression profiles of those markers are well characterized and their role within the context of a particular disease is well understood.

Imaging can be used to help characterize these roles. In this study, we demonstrate that non-invasive imaging of OX40<sup>+</sup> activated T cells has the potential to be a suitable biomarker of early response in cancer immunotherapy. We also describe the successful development of an ImmunoPET agent;  $^{64}\text{Cu}$ -DOTA-AbOX40, capable of detecting OX40 expression with high sensitivity and specificity. We chose a murine OX40 specific IgG1 which upon modification with DOTA retained its immune-reactivity. Bio-conjugation and subsequent radiolabelling with Copper-64 were both facile and reproducible. Cell culture and in vivo binding of the radiotracer, directly

correlated with expression of the biological target, as rigorously characterized by FACS analysis. In our in vivo studies using a murine two-tumor site subcutaneous lymphoma model in which an intra-tumoral vaccine of CpG was administered into only one of the tumors, we identified CD4 OX40<sup>+</sup> T cells as playing an important role in the local tumor and TDLN following vaccination with in situ CpG. The expansion of this OX40 T cell subset may further benefit from combination therapy with an OX40 agonist as recently demonstrated by Sagiv-Barfi et al (35). The authors of the study also demonstrated that CpG does not increase CTLA-4 or PD-1 expression, and that an OX40 agonist alone significantly boosts therapeutic efficacy and leads to complete tumor eradication (35). More recent work has shown that the timing of PD-1 administration can either aid or impair treatment with OX40 (36). As demonstrated here, ImmunoPET can provide insight into these spatiotemporal dynamics and help drive rational drug development and combination strategies.

To realize the full power of ImmunoPET, and improve clinical decision-making, image-derived biomarkers should ideally be combined with other blood-based biomarkers and genetic tests. Utilizing multiple image-derived biomarkers is especially important when imaging *immune response*, where sites such as lymph nodes and spleen can provide additional clues to patient *therapeutic response*. The classifier utilized in this work is only a simple proof of concept, and we plan to test support vector machines and other approaches to see if we can further refine the outcome. Blood based biomarkers performed poorly in the context of monitoring multiple lesions. By contrast, the whole-body spatial information that imaging provides is especially important when utilizing in situ approaches, where the optimal follow-up may warrant injection into non-responding sites. Integrating blood, tissue biopsy and imaging assays with improvements in computational and statistical learning algorithms represents a powerful diagnostic/prognostic patient management approach.

Our data supports OX40 as a highly promising biomarker for imaging activated T cells in vivo with OX40-ImmunoPET representing a readily translatable strategy that can be integrated into the clinical workflow to aid prediction of response, possibly much earlier than current methods allow. The murine antibody imaging strategy described here can be readily adapted to human antibodies for OX40 that are being used for therapy, for OX40 imaging in the clinic. The potential for this strategy could also extend beyond immunotherapies with utility in a number of T cell driven disease indications such as Multiple Sclerosis (37) and Graft Versus Host Disease (38, 39) where expression of this marker has been reported. ImmunoPET strategies will further benefit from the development of second generation agents such as engineered binders that have improved pharmacokinetic properties (e.g. faster blood clearance, lower hepatic accumulation) and are compatible with shorter-lived isotopes, allowing one to image soon after administering tracer and achieving higher signal to background. We are currently pursuing these other avenues to address

the breadth of possible applications in a number of disease models. Based on the promise shown in these preclinical studies, we have started clinical translation of OX40 ImmunoPET.

## **METHODS**

### **Study Design**

The primary objective of this study was to develop an imaging agent ( $^{64}\text{Cu}$ -DOTA-AbOX40) to noninvasively measure OX40 expression with PET imaging, in a dual tumor mouse model treated with an in situ adjuvant vaccine. Mice with dual A20 tumors were size-matched before treatment initiation and received either CpG or vehicle in the left shoulder tumor alone. Tumor volumes of both treated and distal untreated tumors were measured periodically for mice in both treatment groups to monitor treatment response. Five to seven mice per treatment group were used to evaluate the expression of OX40 using PET at an early and late time point post treatment initiation. Additionally, at the same time points, a separate cohort were analyzed by FACS to evaluate OX40 expression and Luminex<sup>®</sup> for cytokines in the blood. All outliers were included in the analysis, and no data were excluded. Authors were not blinded to the results. A minimum of three experimental replicates were recorded for all in vitro data. Simple or multiple linear regression models were used to assess correlation of biomarkers with outcomes. Unsupervised hierarchical clustering was utilized to assign group labels (i.e. responder/ non-responder) based on tumor growth curves. A k-means nearest-centroid approach was employed to classify tumors based on imaging biomarkers.

### **DOTA conjugation and conjugate characterization**

OX40-DOTA conjugation was performed with DOTA-NHS (Macrocyclics) using established protocols previously described (40). Briefly, DOTA conjugation was first optimized using the murine OX40 monoclonal antibody (clone: OX86, BioXcell) resuspended in PBS at 0.5 mg/ml and then buffer exchanged to metal-free HEPES buffer (pH 8.8) and incubated overnight at 4°C with five, ten or fifteen-fold excess of DOTA-NHS. The reactions were quenched with Tris buffer, buffer exchanged into metal free water to remove excess DOTA-NHS, and concentrated. An aliquot of this solution was set aside for Matrix Assisted Laser Desorption Ionization-Time of Flight Mass Spectrometry (MALDI-TOF) analysis along with a sample of unconjugated OX40 antibody to characterize the average number of chelators per antibody molecule. Briefly, the mean DOTA: mAb ratio was determined by calculating the change in mass seen in Matrix-Assisted Laser Desorption Ionization (AB Sciex 5800 TOF/TOF machine (AB Sciex, Framingham, Mass) equipped with a CovalX high-mass detector, divided by the mass of a single DOTA substituent. An average ratio of 1-3 DOTAs per antibody was achieved for the five-fold excess DOTA reaction and used for all

subsequent conjugation reactions. Following MALDI, the solution of DOTA-Ox40mAb was buffer-exchanged into ammonium acetate buffer (0.1 M, pH 5.5) for Copper-64 labeling. DOTA-conjugate solutions were concentrated using ammonium acetate by ultrafiltration (Vivaspin 2 mL, Sartorius) to 2-3 mg/mL and stored at 4°C prior to radiolabeling.

### **Radiolabeling studies**

Standard radiolabeling procedures were used to radiolabel OX40-DOTA with  $^{64}\text{CuCl}_2$  (University of Wisconsin, Madison, WI, USA) (40).  $^{64}\text{Cu}$ -DOTA-AbOX40 was produced with a specific activity of 5-10 $\mu\text{Ci}/\mu\text{g}$ , with high radiochemical purity (>99%), and labeling efficiency of 60-75% as determined by thin-layer chromatography (TLC). Radio-HPLC was performed to corroborate labeling of the antibody. The final formulation was made up in phosphate-buffered saline (0.1 mol/L NaCl, 0.05 M sodium phosphate, pH 7.4).

In brief, DOTA-Ox40-mAb (100  $\mu\text{g}$ ) in 0.25 mol/L ammonium acetate buffer (0.1 M, pH 5.5) was mixed with pH-balanced  $^{64}\text{CuCl}_2$  solution (37 MBq, pH 5.0-5.5, University of Wisconsin, Madison) at 37°C with gentle shaking at 300 rpm. After a 60-minute incubation period, 0.1 M EDTA (0.5 M, pH 8.0) was added to a final concentration of 0.01 M and incubated at room temperature for 15 min to scavenge unchelated  $^{64}\text{CuCl}_2$  in the reaction mixture. Purification of  $^{64}\text{Cu}$ -DOTA-Ox40-mAb was achieved by G25 Sephadex size-exclusion purification (NAP-5 column). Radiochemical purity was determined by instant thin-layer chromatography with TEC-Control Chromatography strips (Biodex Medical Systems, Shirley, NY), developed in saline, and size-exclusion liquid chromatography with a Phenomenex SEC 3000 column (Torrance, CA, USA) with sodium phosphate buffer [0.1 mol/L, pH 6.8]] at a flow rate of 1.0 mL/min.

### **In situ vaccine mouse model**

Six-eight week old female Balb/c mice were purchased from Charles River Laboratories and maintained according to the guidelines of the Stanford University's Institutional Animal Care and Use Committee (Stanford, CA, USA). A20 cells ( $10 \times 10^6$ ) were implanted subcutaneously on the left and right shoulders. Once tumors had grown to approximately 60-80mm<sup>3</sup> in size, mice were treated in their left shoulder tumor with either 50 $\mu\text{g}$  CpG (SD101 oligonucleotide, Dynavax Technologies) or 50 $\mu\text{L}$  PBS. Mice in the control group received a 50  $\mu\text{L}$  injection of PBS into the left shoulder tumor. Mice were then used for PET imaging, FACs or Luminex<sup>®</sup> analysis, 2 days post-treatment initiation (early therapy time point). A separate cohort of mice also underwent 2 repeats of the same intra-tumoral vaccines on Day 2 and Day 4 after the first treatment. These mice were also used for PET imaging, FACs studies or Luminex<sup>®</sup> analysis on Day 9 after the first therapy administration.

(late therapy time point).

### **Small animal PET/CT, Biodistribution studies and Image analysis**

Small animal PET/CT was performed using a protocol previously reported (40). Mice were anesthetized using isoflurane gas (2.0%–3.0% for induction and 1.5%–2.5% for maintenance).  $^{64}\text{Cu}$ -DOTA-AbOX40 (80-110  $\mu\text{Ci}$ ) was administered intravenously (i.v.) via the tail vein 24 hours after intra-tumoral injections. Two types of blocking studies were performed; A) anti-mouse OX40 mAb (100 $\mu\text{g}$ ; BioXCell) was administered i.v. 30 minutes before radiotracer administration (n=3 CpG-treated mice). B) a separate cohort of mice (n=4 per treatment group) received anti-Horse Radish Peroxidase rat IgG1 isotype control (100 $\mu\text{g}$ ; BioXCell) 15 minutes prior to radiotracer administration to further demonstrate specificity of the probe and to rule out the contribution of the radiotracer binding to Fc receptors rather than to the OX40 target, since CpG treatment leads to increased Fc receptor expression (41).

Static PET scans (10 min) were acquired 4, 16 and 24 hours after  $^{64}\text{Cu}$ -DOTA-OX40 administration. CT images were acquired just before each PET scan to provide an anatomic reference for PET data and attenuation correction of the PET data. Following the completion of the scan 24 hours after tracer administration biodistribution studies were performed to measure blood and tissue associated radioactivity. Briefly, blood was collected via cardiac puncture and various tissues (including left (treated) and right (untreated) tumors, left and right tumor draining lymph nodes, inguinal lymph nodes, kidney, liver, lung, muscle, bone, spleen were collected, weighed and radioactivity was measured using an automated gamma counter (Cobra II; Packard). Radioactivity was decay-corrected to the time of radiotracer injection using diluted aliquots of the initial administered dose as standards. Data is expressed as percentage injected dose per gram of tissue (%ID/g) values.

All PET images were reconstructed using 2 iterations of 3-dimensional ordered subsets expectation maximization algorithm (12 subsets) and 18 iterations of the accelerated version of 3D-MAP (i.e., FASTMAP) – matrix size of  $128 \times 128 \times 159$ . Attenuation correction was applied to dataset from CT image. For quantitation, PET images were co-registered with CT images to generate fused images using the Inveon Research Workplace (IRW) image analysis software (version 4.0; Siemens). PET images were analyzed with Inveon Research Workspace software (Version 4.0). The CT images were used to guide the drawing of 3-dimensional regions of interest (ROIs) around the left and right tumors, the tumor draining lymph nodes (TDLN), muscle, kidney and liver. Percentage of injected dose per gram (%ID/g) was calculated for each ROI. Partial volume

correction (PVC) was not applied.

To analyze the pharmacokinetics of  $^{64}\text{Cu}$ -DOTA-AbOX40, ROIs were drawn over key sites; tumor, heart, liver and kidney for the scans acquired for both treatment groups at 4, 16 and 24 hours post tracer administration. PET signal (%ID/g) for these key sites were plotted over time to observe accumulation or clearance.

### **Statistical Analysis**

General statistical analyses were performed in PRISM (GraphPad). Unpaired 2-tailed Student's t-test, one or two-way ANOVA were utilized for column, multiple column and grouped analyses respectively. Bonferroni post-tests were applied when appropriate to correct for multiple comparisons. P-values less than 0.05 were considered statistically significant. Simple linear regression models were generated in PRISM, while multiple linear regressions were performed in R. Pearson's correlation coefficients and p-values were calculated and reported for all model fits.

### **Study approval**

All procedures performed on animals were approved by Stanford University's Institutional Animal Care and Use Committee (Stanford, CA, USA) and were within the guidelines of humane care of laboratory animals.

### **AUTHOR CONTRIBUTIONS**

I.S.A. and A.T.M conceived and designed research studies, developed methodology, conducted experiments, acquired data, analyzed data, and prepared the manuscript. I.S.B. and D.K.C. developed methodology, conducted experiments and analyzed data. K.W. and O.V. conducted experiments. E.M.J. and M.L.J. developed methodology and provided technical and conceptual advice. R.L. conceived and designed research studies. S.S.G. conceived, designed research studies, and prepared the manuscript.

### **SUPPLEMENTAL MATERIAL**

Supplementary Figure 1. Tracer synthesis and quality control schematic.

Supplementary Figure 2. Study design

Supplementary Figure 3. FACS gating and supporting data

Supplementary Figure 4. Phenotypic characterization of OX40 cells

Supplementary Figure 5. Blood cytokine signatures

Supplementary Figure 6. Cytokine ontology

Supplementary Figure 7. ImmunoPET imaging supporting data

Supplementary Figure 8. Histology

Supplementary Figure 9. Supporting ImmunoPET quantification and imaging controls

Supplementary Movie 1. CpG-treated mouse imaged with OX40 ImmunoPET

Supplementary Movie 2. Vehicle-treated mouse imaged with OX40 ImmunoPET

## **ACKNOWLEDGEMENTS**

The authors would like to acknowledge the Stanford Center for Innovation in In-Vivo Imaging (SCI<sup>3</sup>) and in particular, Drs. Timothy Doyle and Frezghi Habte for supporting the preclinical imaging experiments and image analyses. We also thank the Stanford FACS facility and the Stanford Human Immune Monitoring Core for their expertise. In addition, we would like to thank Dr. Kenneth Lau for assistance with mass spectrometry and Dr. Seung Min-Park for supporting the preparation of this manuscript. This work was supported in part from funding from the Ben & Catherine Ivy Foundation (SSG), the Canary Foundation (SSG), and NCI R01 1 CA201719-02 (S.S.G.) and also from the Leukemia and Lymphoma Society (R.L.).

## **CONFLICT OF INTEREST**

Dr Gambhir is the founder and equity holder of CellSight Inc. that develops and translates multimodality strategies for imaging cell trafficking/transplantation. All other authors have declared that no conflict of interest exists.

## REFERENCES

1. Berraondo P, Labiano S, Minute L, Etxeberria I, Vasquez M, Sanchez-Arreaez A, Teijeira A, and Melero I. Cellular immunotherapies for cancer. *Oncoimmunology*. 2017;6(5):e1306619.
2. Kim S, and Moon EK. Development of novel avenues to overcome challenges facing CAR T cells. *Transl Res*. 2017.
3. Finn OJ. Immuno-oncology: understanding the function and dysfunction of the immune system in cancer. *Ann Oncol*. 2012;23 Suppl 8(viii6-9).
4. Hanahan D, and Weinberg RA. Hallmarks of cancer: the next generation. *Cell*. 2011;144(5):646-74.
5. Neves AA, and Brindle KM. Assessing responses to cancer therapy using molecular imaging. *Biochim Biophys Acta*. 2006;1766(2):242-61.
6. Wolchok JD, Hoos A, O'Day S, Weber JS, Hamid O, Lebbe C, Maio M, Binder M, Bohnsack O, Nichol G, et al. Guidelines for the evaluation of immune therapy activity in solid tumors: immune-related response criteria. *Clin Cancer Res*. 2009;15(23):7412-20.
7. Hodi FS, Hwu WJ, Kefford R, Weber JS, Daud A, Hamid O, Patnaik A, Ribas A, Robert C, Gangadhar TC, et al. Evaluation of Immune-Related Response Criteria and RECIST v1.1 in Patients With Advanced Melanoma Treated With Pembrolizumab. *J Clin Oncol*. 2016;34(13):1510-7.
8. Basu S, Chryssikos T, Moghadam-Kia S, Zhuang H, Torigian DA, and Alavi A. Positron emission tomography as a diagnostic tool in infection: present role and future possibilities. *Semin Nucl Med*. 2009;39(1):36-51.
9. Stelljes M, Hermann S, Albring J, Kohler G, Loffler M, Franzius C, Poremba C, Schlosser V, Volkmann S, Opitz C, et al. Clinical molecular imaging in intestinal graft-versus-host disease: mapping of disease activity, prediction, and monitoring of treatment efficiency by positron emission tomography. *Blood*. 2008;111(5):2909-18.
10. Laing RE, Nair-Gill E, Witte ON, and Radu CG. Visualizing cancer and immune cell function with metabolic positron emission tomography. *Curr Opin Genet Dev*. 2010;20(1):100-5.
11. Radu CG, Shu CJ, Nair-Gill E, Shelly SM, Barrio JR, Satyamurthy N, Phelps ME, and Witte ON. Molecular imaging of lymphoid organs and immune activation by positron emission tomography with a new [18F]-labeled 2'-deoxycytidine analog. *Nat Med*. 2008;14(7):783-8.
12. Ronald JA, Kim BS, Gowrishankar G, Namavari M, Alam IS, D'Souza A, Nishikii H, Chuang HY, Ilovich O, Lin CF, et al. A PET Imaging Strategy to Visualize Activated T Cells in Acute Graft-versus-Host Disease Elicited by Allogenic Hematopoietic Cell Transplant. *Cancer Res*. 2017;77(11):2893-902.
13. Keu KV, Witney TH, Yaghoubi S, Rosenberg J, Kurien A, Magnusson R, Williams J, Habte F, Wagner JR, Forman S, et al. Reporter gene imaging of targeted T cell immunotherapy in recurrent glioma. *Sci Transl Med*. 2017;9(373).
14. Freise AC, and Wu AM. In vivo imaging with antibodies and engineered fragments. *Mol Immunol*. 2015;67(2 Pt A):142-52.
15. Galon J, Costes A, Sanchez-Cabo F, Kirilovsky A, Mlecnik B, Lagorce-Pages C, Tosolini M, Camus M, Berger A, Wind P, et al. Type, density, and location of immune cells within human colorectal tumors predict clinical outcome. *Science*. 2006;313(5795):1960-4.
16. Klein O, Ebert LM, Nicholaou T, Browning J, Russell SE, Zuber M, Jackson HM, Dimopoulos N, Tan BS, Hoos A, et al. Melan-A-specific cytotoxic T cells are associated with tumor regression and autoimmunity following treatment with anti-CTLA-4. *Clin Cancer Res*. 2009;15(7):2507-13.
17. Tavare R, Escuin-Ordinas H, Mok S, McCracken MN, Zettlitz KA, Salazar FB, Witte ON, Ribas A, and Wu AM. An Effective Immuno-PET Imaging Method to Monitor CD8-Dependent Responses to Immunotherapy. *Cancer Res*. 2016;76(1):73-82.
18. Rashidian M, Ingram JR, Dougan M, Dongre A, Whang KA, LeGall C, Cragnolini JJ, Bieri B, Gostissa M, Gorman J, et al. Predicting the response to CTLA-4 blockade by longitudinal noninvasive monitoring of CD8 T cells. *J Exp Med*. 2017.

19. Larimer BM, Wehrenberg-Klee E, Dubois F, Mehta A, Kalomeris T, Flaherty K, Boland G, and Mahmood U. Granzyme B PET Imaging as a Predictive Biomarker of Immunotherapy Response. *Cancer Res.* 2017;77(9):2318-27.
20. Spitzer MH, Carmi Y, Reticker-Flynn NE, Kwek SS, Madhireddy D, Martins MM, Gherardini PF, Prestwood TR, Chabon J, Bendall SC, et al. Systemic Immunity Is Required for Effective Cancer Immunotherapy. *Cell.* 2017;168(3):487-502 e15.
21. Zanetti M. Tapping CD4 T cells for cancer immunotherapy: the choice of personalized genomics. *J Immunol.* 2015;194(5):2049-56.
22. Di Galleonardo V, Signore A, Glaudemans AW, Dierckx RA, and De Vries EF. N-(4-18F-fluorobenzoyl)interleukin-2 for PET of human-activated T lymphocytes. *J Nucl Med.* 2012;53(5):679-86.
23. Willoughby J, Griffiths J, Tews I, and Cragg MS. OX40: Structure and function - What questions remain? *Mol Immunol.* 2017;83(13-22).
24. Huet S, Groux H, Caillou B, Valentin H, Prieur AM, and Bernard A. CD44 contributes to T cell activation. *J Immunol.* 1989;143(3):798-801.
25. Wieland E, and Shipkova M. Lymphocyte surface molecules as immune activation biomarkers. *Clin Biochem.* 2016;49(4-5):347-54.
26. Marabelle A, Kohrt H, Caux C, and Levy R. Intratumoral immunization: a new paradigm for cancer therapy. *Clin Cancer Res.* 2014;20(7):1747-56.
27. Wang S, Campos J, Gallotta M, Gong M, Crain C, Naik E, Coffman RL, and Guiducci C. Intratumoral injection of a CpG oligonucleotide reverts resistance to PD-1 blockade by expanding multifunctional CD8+ T cells. *Proc Natl Acad Sci U S A.* 2016;113(46):E7240-E9.
28. Hanagata N. CpG oligodeoxynucleotide nanomedicines for the prophylaxis or treatment of cancers, infectious diseases, and allergies. *Int J Nanomedicine.* 2017;12(515-31).
29. Brody JD, Ai WZ, Czerwinski DK, Torchia JA, Levy M, Advani RH, Kim YH, Hoppe RT, Knox SJ, Shin LK, et al. In situ vaccination with a TLR9 agonist induces systemic lymphoma regression: a phase I/II study. *J Clin Oncol.* 2010;28(28):4324-32.
30. Weinberg AD, Morris NP, Kovacsovics-Bankowski M, Urba WJ, and Curti BD. Science gone translational: the OX40 agonist story. *Immunol Rev.* 2011;244(1):218-31.
31. Marabelle A, Kohrt H, Sagiv-Barfi I, Ajami B, Axtell RC, Zhou G, Rajapaksa R, Green MR, Torchia J, Brody J, et al. Depleting tumor-specific Tregs at a single site eradicates disseminated tumors. *J Clin Invest.* 2013;123(6):2447-63.
32. Yue J, Chen L, Cabrera AR, Sun X, Zhao S, Zheng F, Han A, Zheng J, Teng X, Ma L, et al. Measuring tumor cell proliferation with 18F-FLT PET during radiotherapy of esophageal squamous cell carcinoma: a pilot clinical study. *J Nucl Med.* 2010;51(4):528-34.
33. Namavari M, Chang YF, Kusler B, Yaghoubi S, Mitchell BS, and Gambhir SS. Synthesis of 2'-deoxy-2'-[18F]fluoro-9-beta-D-arabinofuranosylguanine: a novel agent for imaging T-cell activation with PET. *Mol Imaging Biol.* 2011;13(5):812-8.
34. Franc BL, Goth S, MacKenzie J, Li X, Blecha J, Lam T, Jivan S, Hawkins RA, and VanBrocklin H. In Vivo PET Imaging of the Activated Immune Environment in a Small Animal Model of Inflammatory Arthritis. *Mol Imaging.* 2017;16(1536012117712638).
35. Sagiv-Barfi I, Czerwinski DK, Levy S, Alam IS, Mayer AT, Gambhir SS, and Levy R. Eradication of spontaneous malignancy by local immunotherapy. *Science translational medicine.* 2018;10(426).
36. Shrimali RK, Ahmad S, Verma V, Zeng P, Ananth S, Gaur P, Gittelman RM, Yusko E, Sanders C, Robins H, et al. Concurrent PD-1 Blockade Negates the Effects of OX40 Agonist Antibody in Combination Immunotherapy through Inducing T-cell Apoptosis. *Cancer Immunol Res.* 2017;5(9):755-66.
37. Carboni S, Aboul-Enein F, Waltzinger C, Killeen N, Lassmann H, and Pena-Rossi C. CD134 plays a crucial role in the pathogenesis of EAE and is upregulated in the CNS of patients with multiple sclerosis. *J Neuroimmunol.* 2003;145(1-2):1-11.
38. Kotani A, Ishikawa T, Matsumura Y, Ichinohe T, Ohno H, Hori T, and Uchiyama T. Correlation of peripheral blood OX40+(CD134+) T cells with chronic graft-versus-host

- disease in patients who underwent allogeneic hematopoietic stem cell transplantation. *Blood*. 2001;98(10):3162-4.
39. Paz Morante M, Briones J, Canto E, Sabzevari H, Martino R, Sierra J, Rodriguez-Sanchez JL, and Vidal S. Activation-associated phenotype of CD3 T cells in acute graft-versus-host disease. *Clin Exp Immunol*. 2006;145(1):36-43.
  40. James ML, Hoehne A, Mayer AT, Lechtenberg K, Moreno M, Gowrishankar G, Ilovich O, Natarajan A, Johnson EM, Nguyen J, et al. Imaging B cells in a mouse model of multiple sclerosis using <sup>64</sup>Cu-Rituximab-PET. *J Nucl Med*. 2017.
  41. Krieg AM, Yi AK, Matson S, Waldschmidt TJ, Bishop GA, Teasdale R, Koretzky GA, and Klinman DM. CpG motifs in bacterial DNA trigger direct B-cell activation. *Nature*. 1995;374(6522):546-9.

## FIGURES

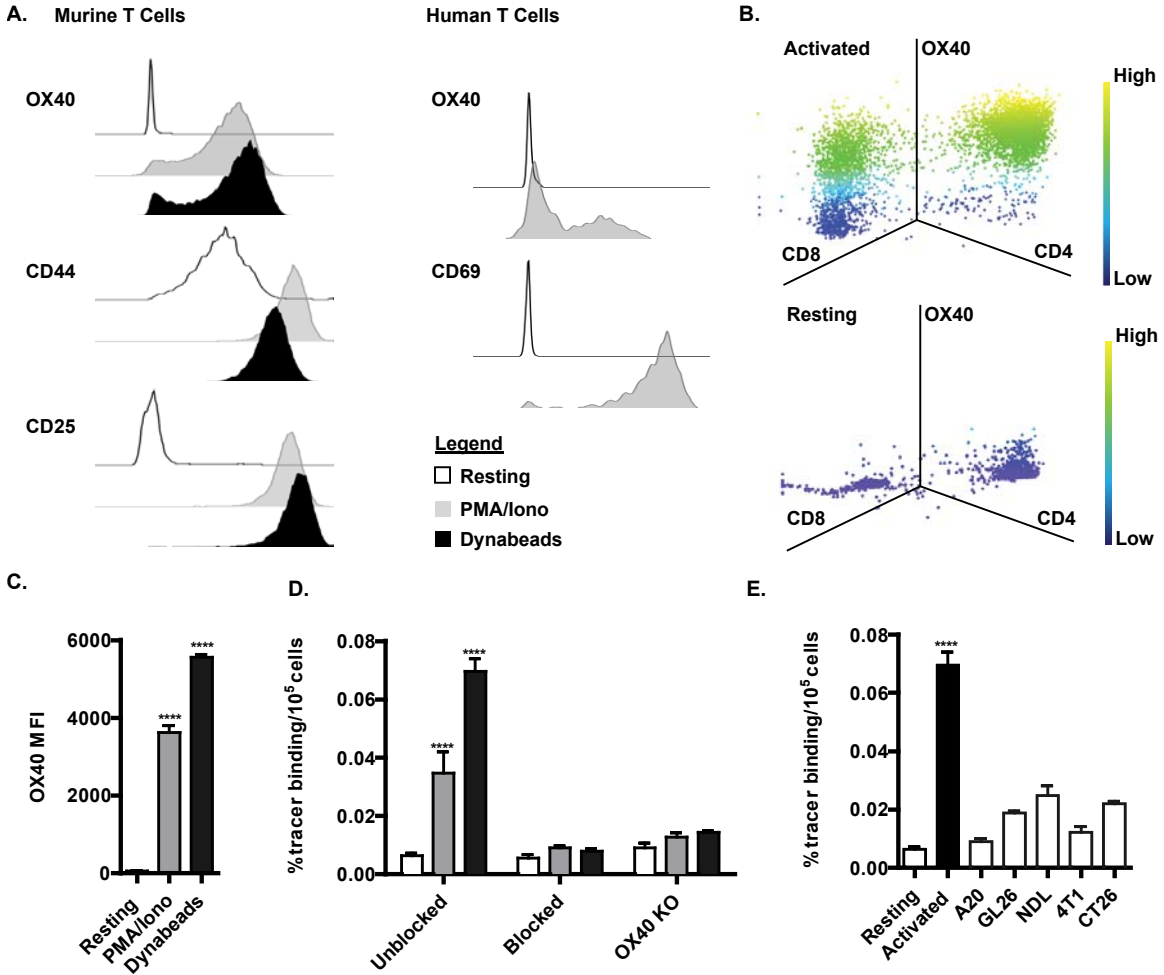


**Figure 1. OX40 is a sensitive and specific indicator of T cell activation in vitro.** **A)** Left: Histograms (fluorescence intensity) for OX40, CD44 and CD25 expression following murine T cell activation with PMA/Ionomycin or CD3/CD28 specific antibody-coated Dynabeads. Right: Histograms (fluorescence intensity) for human T cells following activation. **B)** Three-dimensional flow cytometry plots of OX40 expression on resting and activated CD4 and CD8 murine T cell subsets. Scale bar: Purple = low OX40 expression; Yellow = high OX40 expression. **C)** Quantitation of OX40 mean fluorescence intensity (MFI) from resting, PMA/Ionomycin or Dynabead activated murine T cells (n=3 mice/group). **D)** Corresponding <sup>64</sup>Cu-DOTA-AbOX40 tracer uptake (% dose/10<sup>5</sup> cells) in resting, PMA/Ionomycin or Dynabead activated murine T cells (n=6 mice/group) for unblocked, blocked and knock out (KO) groups from two independent experiments. **E)** <sup>64</sup>Cu-DOTA-AbOX40 tracer uptake (% dose/10<sup>5</sup> cells) in Dynabead activated murine T cells compared to resting T cells and various murine cancer cell lines (n=3 mice/group). A20: B cell lymphoma; GL26: glioma; All procedures performed on animals were approved by Stanford University's Institutional

Animal Care and Use Committee and were within the guidelines of humane care of laboratory animals. A20: B cell lymphoma; GL26: glioma; NDL: mammary; 4T1: mammary carcinoma; CT26: colorectal carcinoma. All values represent mean  $\pm$  SEM unless specified. Two-way ANOVA with Bonferroni post-test for grouped comparisons; else one-way ANOVA \*\*\*\*,  $p < 0.0001$ ; \*\*\*,  $p < 0.001$ ; \*\*,  $p < 0.01$ ; \*,  $p < 0.05$

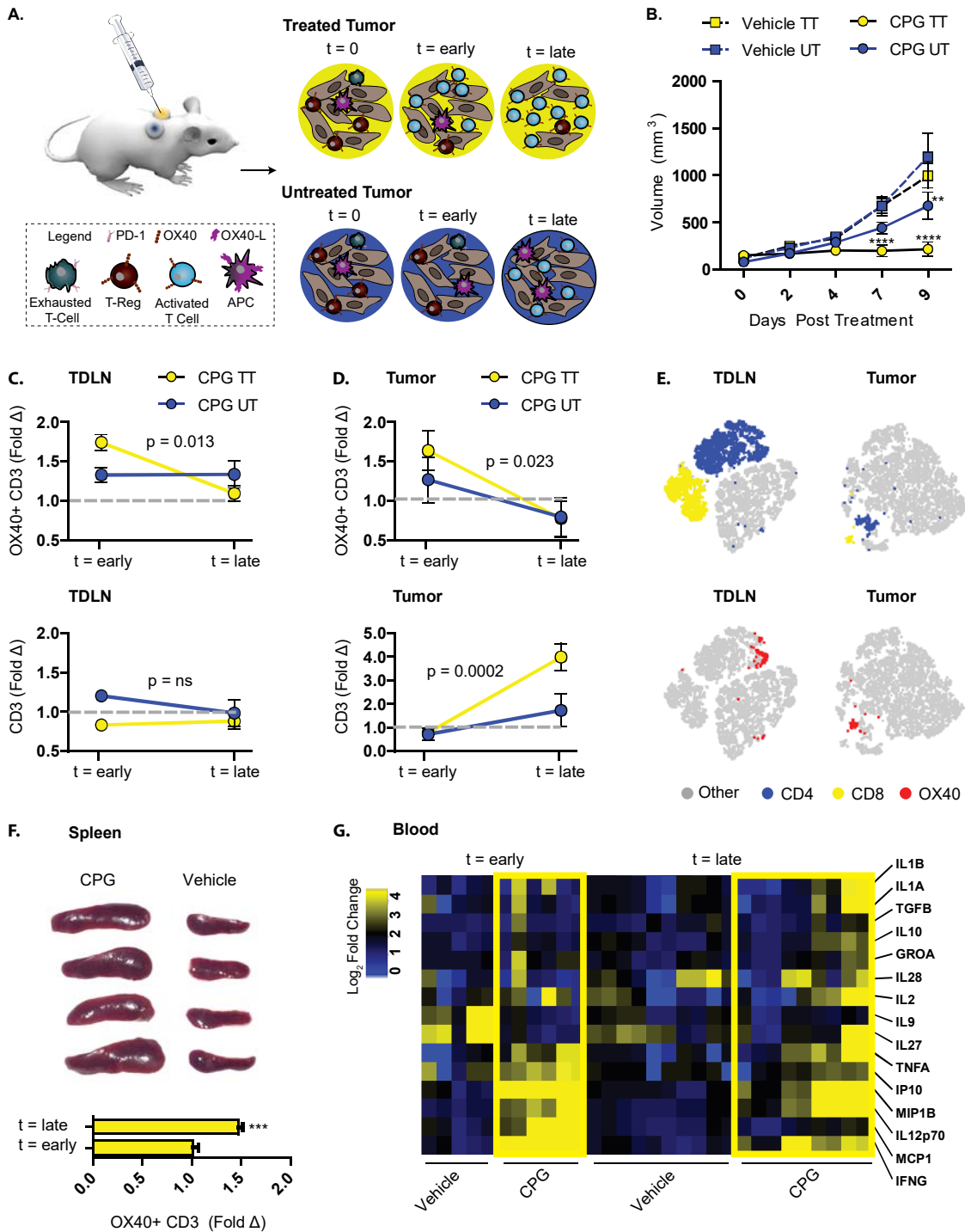


**Figure 2. In situ vaccination with CpG activates OX40 T cells in the local tumor and tumor draining lymph node leading to the onset of a systemic response. A)** Schematic representation of in situ vaccination strategy and a hypothetical immune response **B)** Treated (TT) and untreated (1) tumor growth curves (volume; mm<sup>3</sup>) based on caliper measurements for CpG (n=7) and Vehicle (n=8) cohorts. Values represent mean ± SEM. Two-way ANOVA with Bonferroni

post-test; \*\*\*\*,  $p < 0.0001$ ; \*\*,  $p < 0.01$  **C)** Top: Fold change (normalized to Vehicle) in frequency of OX40<sup>+</sup> CD3<sup>+</sup> T cells in CpG-treated vs. untreated tumor draining lymph node (TDLN) and **D)** tumor at early (n=5 mice/group) and late (n=4 mice/group) time points. Bottom: Fold change in frequency of CD3<sup>+</sup> T cells. Gray dashed line demarcates unity. Values represent mean  $\pm$  SEM. Two-way ANOVA; p-values represent probability differences over time in marker expression are due to random chance. **E)** Representative ViSNE clustering of CD4, CD8 and OX40 markers at early time point, CpG cohort. **F)** Top: Images of spleens (late timepoint) from CpG and Vehicle cohorts taken side by side. Bottom: Fold change (normalized to Vehicle) in frequency of OX40<sup>+</sup> CD3 T cells in CpG-treated cohort at early (n=5 mice) and late (n=4 mice) time points. Unpaired student's T-test; \*\*\*,  $p < 0.001$  **G)** Heatmap of  $\log_2$  fold change (normalized to control mice) in cytokine expression at both early and late time points in vehicle and CpG-treated cohorts. Columns: mice, Rows: cytokines. Scale bar: Blue = 0, Yellow > 4  $\log_2$  fold change.

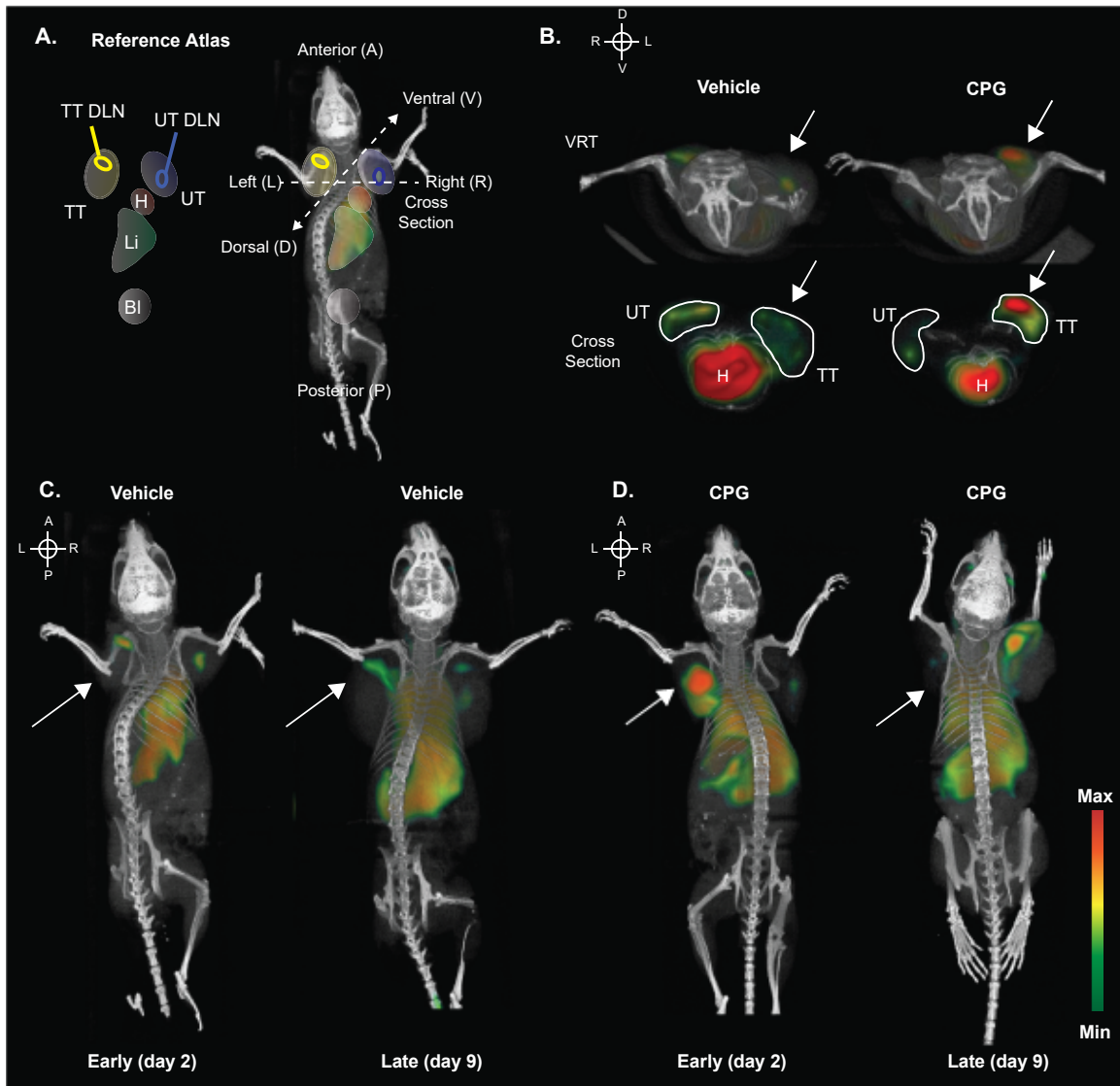


**Figure 3. Noninvasive imaging of OX40 captures the spatiotemporal dynamics of activated T cells following in situ vaccination.** All images acquired 24h post  $^{64}\text{Cu}$ -DOTA-AbOX40 tracer injection [ $\sim 100\mu\text{Ci}$ ]. **A)** Reference atlas for image regions of interest (ROIs). TT DLN: Treated tumor draining lymph node; UT DLN: Untreated tumor draining lymph node; TT: Treated tumor; UT: Untreated tumor; H: Heart; Li: Liver; BI: Bladder. **B)** Top: Head on-view of volume rendered technique (VRT) PET/CT images of representative mice vaccinated in situ with either vehicle or CpG. Bottom: Axial cross section through tumors and heart. Images acquired on day 2 post therapy **C.** VRT PET/CT images of representative vehicle and **D.** CpG-treated mice at day 2 and day 9 post vaccination. White arrows indicate treatment site. Scale bar: Max = Red, Min = Green.

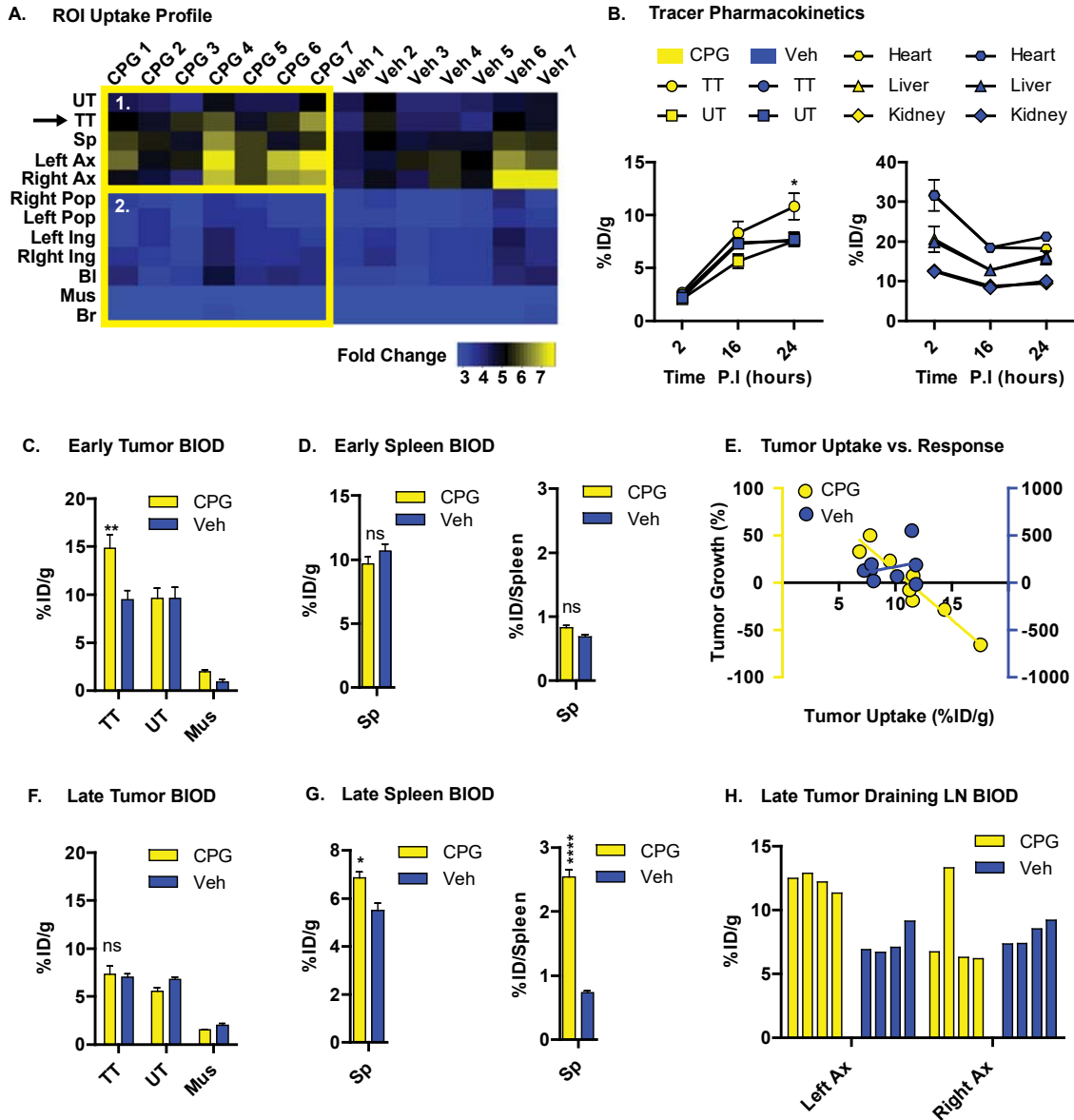


**Figure 4. Quantitative ImmunoPET tracer pharmacokinetics and biodistribution.** **A)** Early (day 2) post therapy  $^{64}\text{Cu}$ -DOTA-AbOX40 uptake profile [Fold change:  $\% \text{ID/g ROI} / \% \text{ID/g Muscle}$ ; no PVC] in CpG (n=7 mice) vs. Vehicle (Veh, n=7 mice) treated mice at 24 hours post-injection [100  $\mu\text{Ci}$ ]. UT: untreated tumor; TT: treated tumor; Sp: spleen; Ax: axillary lymph node; Pop: popliteal lymph node; Ing: inguinal lymph node; Bl: bladder; Mus: muscle; Br: brain. Two distinct clusters of image biomarkers, labeled 1 and 2, were identified from unsupervised hierarchical clustering. **B)**  $^{64}\text{Cu}$ -DOTA-AbOX40 pharmacokinetic uptake and clearance [ $\% \text{ID/g}$ ] in CpG (n=3 mice) vs. Vehicle (n=3 mice) mice cohorts at 2, 16, and 24h post-injection **C)** Early (day 2)  $^{64}\text{Cu}$ -DOTA-AbOX40 biodistribution (BIOD) uptake [ $\% \text{ID/g}$ ] in treated tumors vs. untreated tumors and background muscle. **D)** Early (day 2)  $^{64}\text{Cu}$ -DOTA-AbOX40 BIOD uptake in spleen [ $\% \text{ID/g}$ ,  $\% \text{ID/spleen}$ ]. **E)** Early (day 2) tumor response (% change volume) vs. day 2 tumor  $^{64}\text{Cu}$ -DOTA-

AbOX40 uptake (%ID/g BIOD). Generalized linear regression. CpG:  $y = -10.3x + 115.3$ ,  $r^2: 0.9141$ ; Veh:  $y = 22.2x - 54.1$ ,  $r^2: 0.06$ ; Y-axis 1: yellow/ CpG, Y-axis 2: blue/Veh **F-G**) Late (day 9)  $^{64}\text{Cu}$ -DOTA-OX40 uptake in tumors, spleen and muscle [%ID/g, %ID/spleen, BIOD]. **H**) Late (day 9) uptake in left and right axillary lymph nodes of individual CpG and Veh mice [%ID/g, BIOD]. All values represent mean +/- SEM unless specified. Two-way ANOVA with Bonferroni post-test for multiple comparisons; else student's t-test \*\*\*\*,  $p < 0.0001$ ; \*\*\*,  $p < 0.001$ ; \*\*,  $p < 0.01$ ; \*,  $p < 0.05$

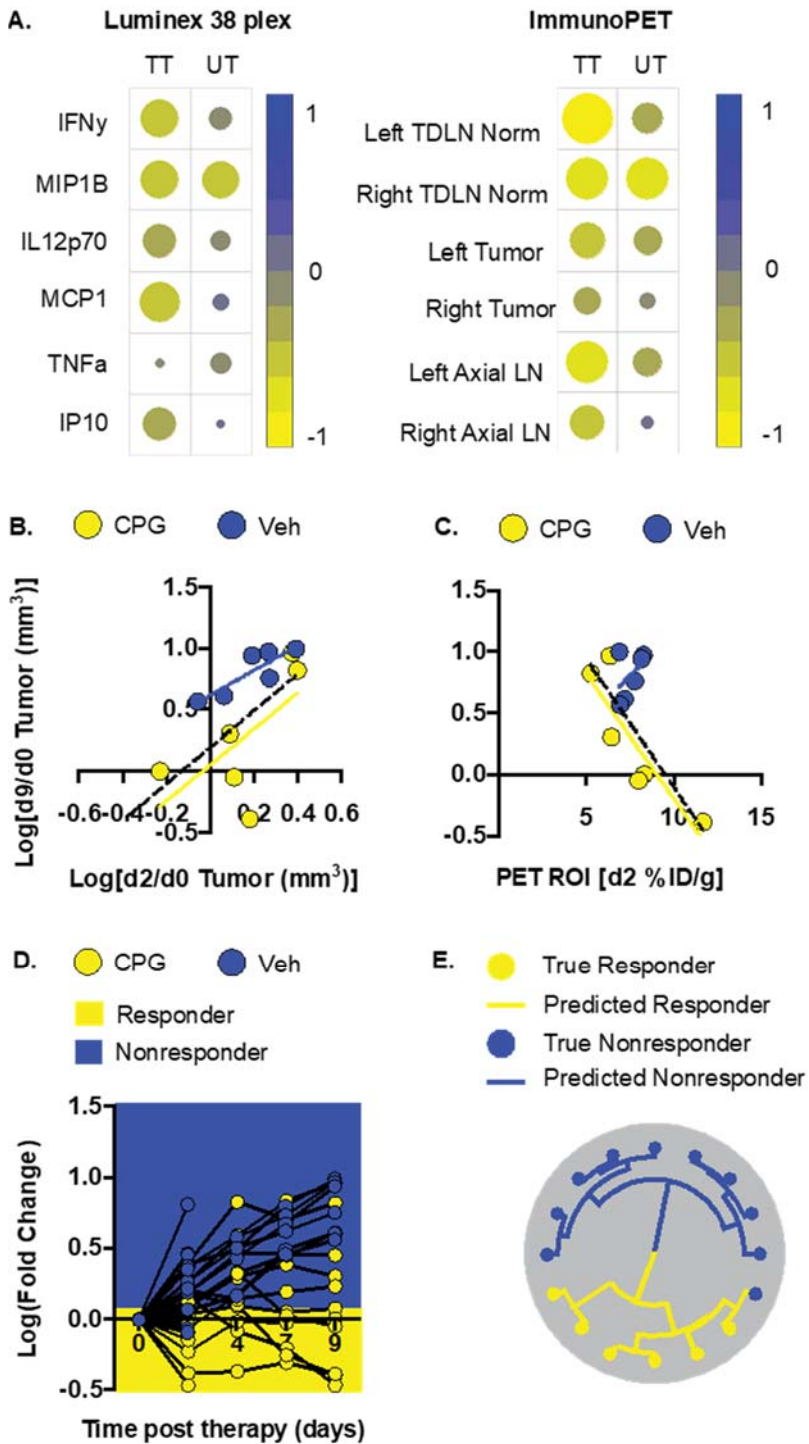


**Figure 5. Imaging and blood-based correlates of response to in situ tumor vaccination with CpG** **A)** Correlelogram of top hits determined by significance analysis of microarrays from Luminex 38 plex cytokine assay [Fold change; MFI/ctl] and ImmunoPET imaging regions of interest [Fold change; %ID/g ROI/muscle] with tumor response day 2 ( $\log[\text{fold}(\text{tumor vol mm}^3 \text{ d2: tumor vol mm}^3 \text{ d0})]$ ). Color scale and circle size both represent Pearson's correlation coefficients. Large

yellow circle (-1): Perfect inverse-correlation, no circle (0): no correlation, large blue circle (1): perfect correlation **B)** Univariate regression of day 9 tumor response vs. day 2 tumor response made via anatomical measurements. **C)** Univariate regression of day 9 tumor response vs. day 2 tumor tracer uptake [%ID/g]. Blue line: Vehicle only fit; Yellow line: CpG only fit; Black dashed line: All. **D)** Tumor growth vs. time post therapy. Yellow zone designates responders. Cut-off determined using unsupervised hierarchical clustering **E)** Unsupervised hierarchical clustering and model visualization of k-means nearest centroid classifier. Lines – predictions. Circles - truth

**Table 1. Correlates of Early Tumor Response**

	PET (n=28)	Luminex (n=12)
Model	Mul GLM	Mul GLM
y	Log(d2/d0 mm <sup>3</sup> )	Log(d2/d0 mm <sup>3</sup> )
x1, x2, x3 ...	See legend	See legend
Res Std Error	0.162	0.127
Deg of Freedom	22	7
R-squared	0.674	0.405
P-value	8.425e-05	0.393

Multivariate general linear regression model (Mul GLM). PET predictors x1, x2, x3: TDLN normalized to tumor size (mean %ID/g: mm<sup>3</sup>), Tumor (mean %ID/g), Axillary lymph node (mean %ID/g), Inguinal lymph node (mean %ID/g), Popliteal lymph node (mean %ID/g). Luminex predictors x1,x2,x3: IFN $\gamma$ , MIP1B, IL12p70, MCP1. N represents number of tumors.

**Table 2. Predictors of Late Tumor Response**

	Anatomical (n=12)	PET (n=12)	PET (n=12)
Model	Uni GLM	Uni GLM	Mul GLM
Veh (R <sup>2</sup> /p-value)	0.74/0.11	0.23/0.33	N/A
CPG (R <sup>2</sup> /p-value)	0.40/0.18	0.76/0.02	N/A
All (R <sup>2</sup> /p-value)	0.34/0.05	0.39/0.03	0.74/0.08

Correlation coefficient r<sup>2</sup> and p values for model fits. Uni Glm: univariate general linear regression model. Multi GLM: multiple linear regression model. N represents number of tumors.

**Table 3. Classification of Responders vs Nonresponders**

	Train (n=16)	Test (n=30)	Total (n=46)
Model	K-means	K-means	K-means
Accuracy	0.938	0.767	0.826
Sensitivity	0.90	0.71	0.85
Specificity	1.00	0.78	0.82

Accuracy, sensitivity and specificity of training (n=16), testing (n=30) and total (n=46) included in study. N represents number of tumors.